Conversion–Lithiophilicity Hosts Toward Long-Term and High-Energy-Density Lithium Metal Batteries

Aoming Huang, Hongjiao Huang, Shaoxiong Li, Xiansong Pan, Ai-Yin Wang, Han-Yi Chen, Tao Wang, Linlin Li, Maxim Maximov, Jianwei Ren, Yuping Wu, Shengjie Peng

A. Huang, H. Huang, S. Li, X. Pan, L. Li, S. Peng
College of Materials Science and Technology, Nanjing University of Aeronautics and Astronautics, Nanjing 210016, China
E-mail: pengshengjie@nuaa.edu.cn

A.-Y. Wang, H.-Y. Chen
Department of Materials Science and Engineering, National Tsing Hua University, Hsinchu 30013, Taiwan

T. Wang, Y. Wu
Confucius Energy Storage Lab, School of Energy and Environment & Z Energy Storage Center, Southeast University, Nanjing 211189, China
E-mail: wangtao2021@seu.edu.cn;wuyp@seu.edu.cn

M. Maximov
Peter the Great Saint-Petersburg Polytechnic University, Saint-Petersburg 195221, Russia

J. Ren
Department of Chemical Engineering, University of Pretoria, cnr Lynnwood Road and Roper Street, Hatfield 0028, South Africa

Abstract

Lithium metal anode emerges as an ideal candidate for the next generation of high-energy-density batteries. However, challenges persist in achieving high lithium utilization rates while maintaining the demands of high energy density and extended cycle life. In this work, a novel conversion–lithiophilicity strategy is proposed to regulate the longevity of high-energy-density batteries by injecting lithium ion activity. This strategy is validated through carbon nanofiber decorated with Fe_3C and Fe_2O_3 particles. The uniform metallic lithium deposition induced by lithiophilic Fe_3C substrates has been verified through lithium deposition/stripping experiments and density functional theory calculations. The electrochemical active Fe_2O_3 component supplies additional anodic capacity and suppress battery degradation, as demonstrated in lithium-ion storage research and three electrode system studies. When paired with $LiFePO_4$ cathodes at an N/P ratio of 2, the full battery showcases outstanding cycling stability over 300 cycles at 1C, with an exceptional energy density of 438 Wh kg^{-1} (calculated based on the cathode material and lithium content). Furthermore, the full battery delivers rapid kinetics of 124 mAh g^{-1} at 2C. The conversion–lithiophilicity strategy presented offers a promising avenue for the development of high-energy density and long-life lithium metal batteries.

1 Introduction

Lithium metal is regarded as a leading candidate for anodes in the forthcoming era of high-energy-density batteries, attributed to its exceptionally high theoretical capacity of 3860 mAh g^{-1} and a low electrode potential of −3.04 V relative to the standard hydrogen electrode.[1] The realization of high energy density, however, necessitates stringent control over lithium

concentration, which must remain below 10 mAh cm^{-2}, and the ratio of negative to positive (N/P) capacity, which should not exceed 3.[2] Although an elevated N/P ratio can bolster the short-term endurance of the battery, it does so at the expense of lithium utilization efficiency and incurs additional costs.[3] Various strategies aimed at modulating the lithium plating and stripping behavior of lithium metal anodes (LMAs), including the design of electrolytes, the construction of functional 3D hosts, and the application of artificial protective films, have yet to fully mitigate challenges such as the formation of dead lithium and the reduction in Coulombic efficiency (CE).[4] Consequently, innovative approaches are urgently needed to achieve a prolonged cycle life for lithium metal batteries while maintaining high energy density.

Functional lithium metal hosts are predicated on lithophilic materials that possess substantial capacities for lithium adsorption, such as certain metals or metal oxides.[5] However, even with lithiophilic anodes, challenges pertaining to steady-state lithium deposition and the longevity of the battery have not been entirely surmounted.[6] Furthermore, there is a scarcity of comprehensive studies on carbide-based compounds, which, despite their beneficial properties like electrical conductivity, have not been extensively explored.[7] The application of electrospinning technology facilitates the creation of custom 3D conductive scaffolds that can significantly diminish the nucleation overpotential, and it also allows for the seamless encapsulation of active substrates within nanofibers for lithium storage.[8] Yet, batteries may still undergo a precipitous decline in capacity, potentially attributable to the aggregation of inactive lithium and the consequent depletion of lithium reserves at the anode.[9] Through reversible replacement redox reactions with Li^+, transition metal cations can achieve substantial lithium-ion storage capacities.[10] When contrasted with lithium metal anodes, the conversion process is characterized by a slightly higher delithiation potential (greater than 0.5 V, versus Li/Li^+) and enhanced reversibility.[11] The potential difference generated by the integrating with metallic lithium can mitigate voltage spikes during near-full charge or deep discharge conditions and provide a buffer for battery power detection.[12] The integration of conversion materials into the lithium metal anode, which are endowed with highly reversible processes for the sequestration and liberation of lithium ions, is anticipated to augment the full cell's conversion efficiency.[13]

Herein, a conversion–lithiophilicity (CL) strategy is introduced to foster the development of lithium metal batteries with extended cycle life and high energy density. This CL strategy integrates lithiophilic hosts that enhance the deposition of metallic lithium with electrochemically active sites capable of storing lithium ions, thereby improving full cell performance. Utilizing electrospun carbon nanofibers embedded with electrochemically active Fe_2O_3 and lithiophilic Fe_3C (referred to as EC-LPF), a prototype has been synthesized to exemplify this concept. Specifically, Fe_3C substrate demonstrates superior lithiophilicity compared to conventional oxides, thereby lowering the nucleation barrier, while the Fe_2O_3 substrate provides additional capacity for lithium-ion storage through a conversion reaction. The lithium storage performance of the battery was validated using a two-electrode full cell configuration, and the dynamic progression of battery failure was elucidated through a three-electrode system. As anticipated, the EC-LPF composite material achieves the lowest nucleation overpotential (12 mV). The Li/EC-LPF symmetric cell exhibits stable cycling performance over more than 400 h with an overpotential as low as 24 mV at a current density of 3 mA cm^{-2} and an areal capacity of 1 mAh cm^{-2}. Furthermore, when paired with a $LiFePO_4$ cathode, the $LiFePO_4$||Li/EC-LPF full cell delivers an exceptionally long cycle life of 300 cycles at a 1C rate, coupled with high-rate capability and an energy density reaching up to 438 Wh kg^{-1} (considering cathode material and lithium content).

2 Results and Discussion

Density functional theory (DFT) was initially utilized to determine the adsorption energy of various carbides on lithium. Models were crafted with lithium integrated into the materials to create a cohesive structure that results in greater stability (**Scheme** 1a,b; Figure S1, details of which are provided in Experimental Section of Supporting Information).[14] It is evident from Scheme 1c that all carbides exhibit robust adsorption, with Fe_3C demonstrating the most significant adsorption energy at −2.57 eV, markedly surpassing that of Fe_2O_3 (−0.62 eV). When compared to lithiophilic iron carbide, iron oxide, a conventional redox lithium-ion anode material, is noted for its exceptionally high capacity for lithium-ion storage.[15] In the context of lithium storage using a conversion–lithiophilicity host, as illustrated in Scheme 1d, lithium initially infuses into the electrochemically active Fe_2O_3 as a provisional storage site, followed by the deposition of metallic lithium under the influence of lithiophilic Fe_3C. As the accumulation of dead lithium occurs, the pre-stored lithium ions in Fe_2O_3, which represent the reversible lithium-ion capacity generated through the conversion reaction, are gradually released back into the cycle, thus preventing severe battery degradation. The combined effect of the conversion mechanism of Fe_2O_3 and the potent lithiophilicity of Fe_3C serves to prolong the cycle life of lithium metal batteries through distinct lithium storage mechanisms under a gradient potential (Scheme 1e).

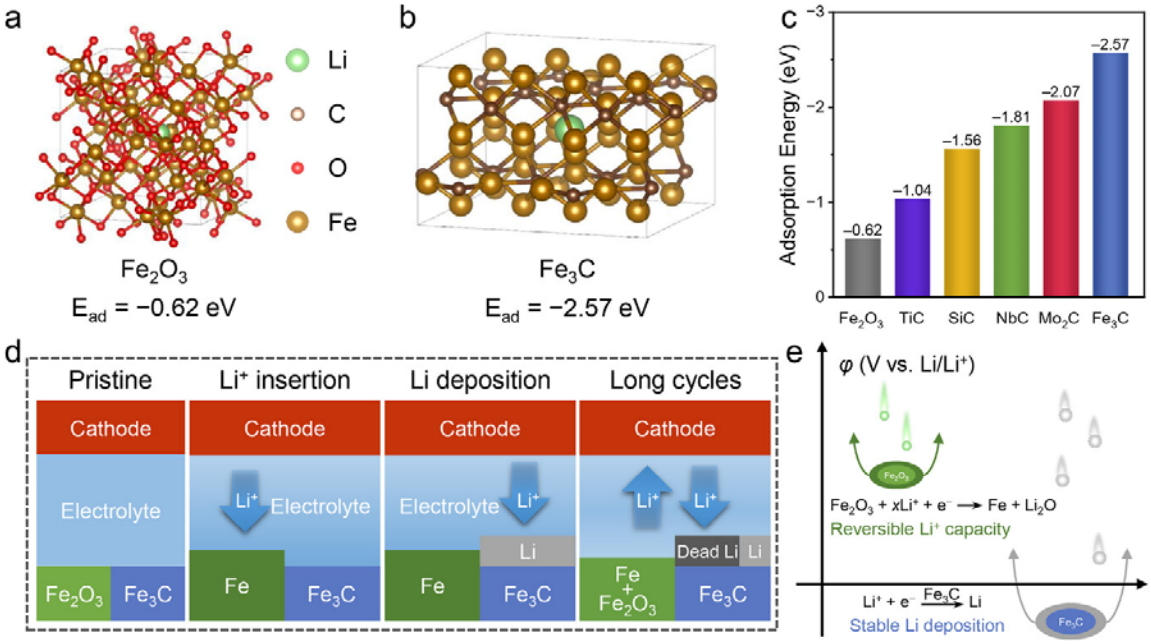

Scheme 1. The adsorption structure and the corresponding adsorption energy of Li in a) Fe_2O_3 and b) Fe_3C. c) The adsorption energy of Li in common carbides. d) Schematic diagram of the conversion–lithiophilicity mechanism based on EC-LPF full battery in its pristine state, Li^+ insertion, Li deposition, and after long cycles, as well as e) its redox reaction process.

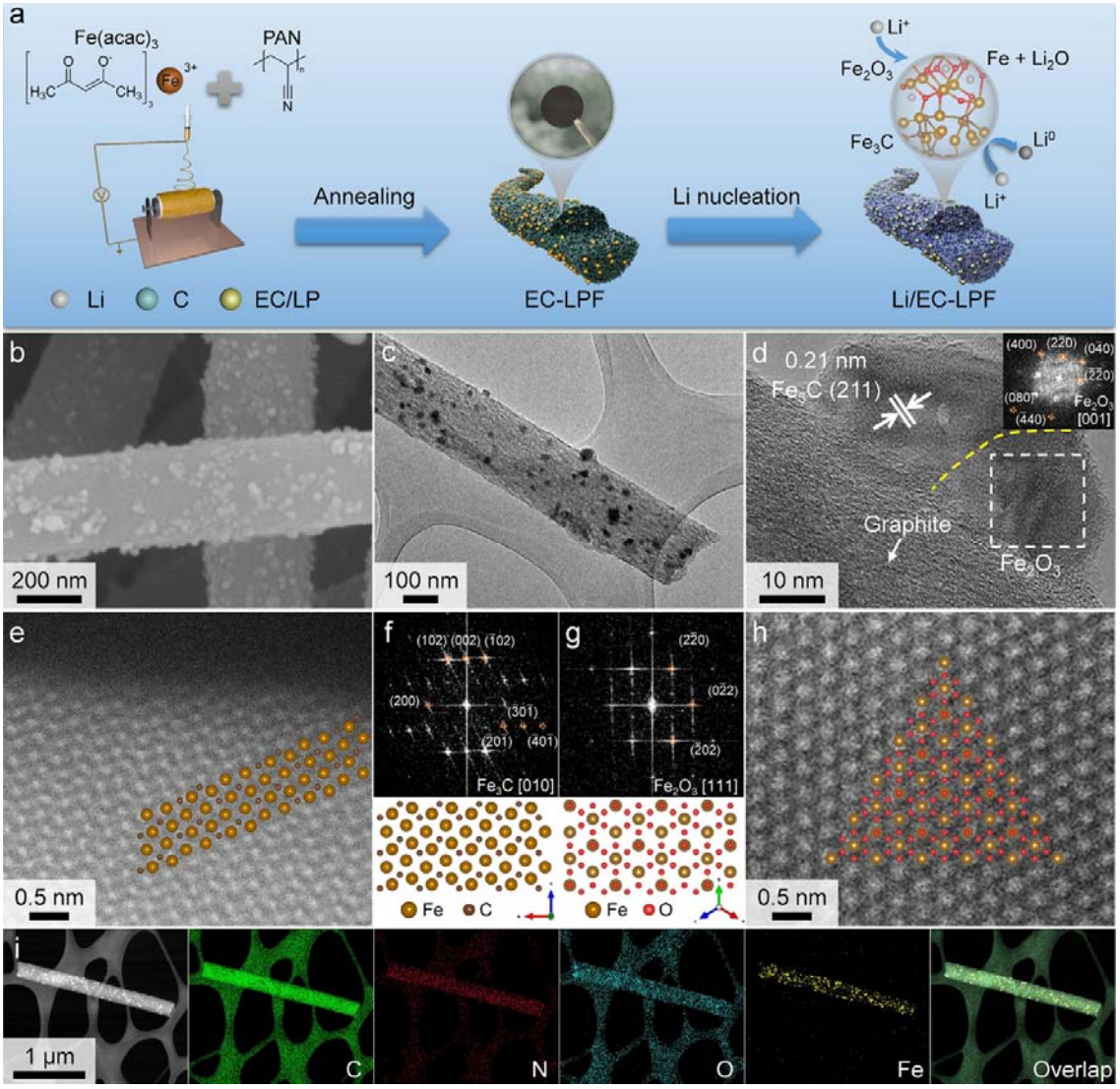

Figure 1. a) Schematic diagram of electrode preparation. b) SEM and c,d) TEM images of EC-LPF, inset: corresponding FFT pattern of the squared region highlighted in (d). AC-STEM image and corresponding FFT pattern and atomic structure of e,f) Fe_3C and g,h) Fe_2O_3 in EC-LPF. i) EDS elemental mappings of EC-LPF.

The self-supporting EC-LPF membrane is fabricated through electrospinning technology and subsequent treatment, as outlined in **Figure** 1a (see Experimental Section of Supporting Information). During the subsequent lithium storage process, Fe_2O_3 within the self-supporting materials absorbs lithium ions to pre-store a portion of the capacity, while Fe_3C induces uniform lithium deposition, thereby synergistically achieving secure and enduring operation of lithium metal anodes. The prepared EC-LPF possesses a uniform diameter of ≈300 nm through scanning electron microscopy (SEM) images (Figure 1b; Figure S2, Supporting Information), with numerous nanoparticles, ≈20 nm in size, dispersed across its surface. The transmission electron microscopy (TEM) image in Figure 1c demonstrates that fibers not only bear a multitude of particles but also exhibit a rich porous structure, potentially a result of the etching effect of metals on carbon during the annealing process.[16] In addition, high-resolution TEM images (Figure 1d) disclose particles with a lattice spacing of 0.21 nm within numerous

graphitized carbon layers, identifiable as the (211) plane of Fe_3C grains, and the cubic phase Fe_2O_3 oriented along [001], as confirmed by fast Fourier transform (FFT) analysis. Additionally, aberration-corrected scanning transmission electron microscopy (AC-STEM) with a high-angle annular dark-field detector more clearly reveals the Fe_3C phase. The atomic layers depicted in Figure 1e originate from the orderly superposition and arrangement of Fe and C atoms. The corresponding FFT images and atomic structure diagrams (Figure 1f) distinctly indicate the [010] zone axis of Fe_3C. The atomic-level image of Fe_2O_3 oriented toward the [111] zone axis is also observable in Figure 1g,h. An energy dispersive X-ray spectroscopy (EDS) elemental spectrum of an individual EC-LPF fiber (Figure 1i) reveals the uniform distribution of C, N, O, and Fe elements within the microstructure. Lithiophilic Fe_3C on carbon nanofiber (LPF) and electrochemically active Fe_2O_3 on carbon nanofiber (ECF) are prepared using analogous procedures at identical annealing temperature, with the aim of neutralizing the direct impact of temperature on the degree of graphitization of carbon materials, thereby influencing their electrical conductivity and lithium deposition performance.[17] Apart from the distinct pores formed by metal etching due to H_2 reduction on the ECF surface, the comparative sample exhibits a similar fiber morphology and porous structure (Figures S3 and S4, Supporting Information).[18]

A comprehensive series of characterizations were conducted to ascertain the composition and structural attributes of the self-supporting electrospun fibers. Initially, the X-ray diffraction (XRD) patterns of LPF and ECF in **Figure** 2a can be characterized as orthorhombic Fe_3C phase (JCPDS card no. 35–0772) and cubic Fe_2O_3 phase (JCPDS card no. 39–1346), respectively. EC-LPF clearly demonstrates a good combination of these two phases, accompanied by a pronounced graphitized carbon peak. The characteristic D and G bands of carbon in Raman spectroscopy substantiate this observation (Figure 2b). Specifically, the D/G ratios for LPF, ECF, and EC-LPF are 1.05, 1.11, and 0.97, respectively. A heightened degree of graphitization in carbon materials is advantageous for electron conduction.[19] Thermogravimetric (TG) analysis indicates that Fe_3C constitutes 16.6% by weight of LPF, and Fe_2O_3 makes up ≈38% by weight of ECF (Figure 2c). The calculated mass of each component of EC-LPF reveals that Fe_3C and Fe_2O_3 account for 14.4% and 14.7%, respectively. The surface chemical composition and elemental states of Fe-based electrospun fibers were investigated using X-ray photoelectron spectroscopy (XPS). The high-resolution Fe 2p spectrum in Figure 2d displays peaks at 707.3, 711.2, and 714.7 eV, attributable to Fe–C, Fe^{2+}, and Fe^{3+}, respectively, aligning with their corresponding substances.[20] Moreover, following the formation of heterostructures, the electron cloud overlap results in a reduction of the inter-peak distance from 4.0 to 3.5 eV. In the high-resolution N 1s spectrum (Figure 2e), N-doped carbon, particularly pyridine N, exhibits a higher binding energy and a stronger capacity for lithium-ion adsorption, which will modulate the nucleation and growth characteristics of lithium.[21] Additionally, a substantial amount of graphitized N is presumed to enhance the conductivity of self-supporting materials.[22] The porous characteristics of the prepared electrospun fiber material were further quantified through specific surface area measurements. The nitrogen adsorption/desorption isotherm exhibits a type IV characteristic curve with a multitude of microporous structures (Figure 2f). The Brunauer Emmett Teller (BET) surface areas for LPF, ECF, and EC-LPF are 241, 404, and 137 $m^2 g^{-1}$, respectively. The substantial specific surface area of ECF is attributed to its increased number of micropores and a broader distribution of mesopores, as derived from the Barrett-Joyner-Halenda (BJH) model (Figure S5, Supporting Information). In addition to the high specific surface area contributed by micropores, electrospun fibers also possess a higher outer surface, which aids in augmenting the contact area and reducing the effective current density.

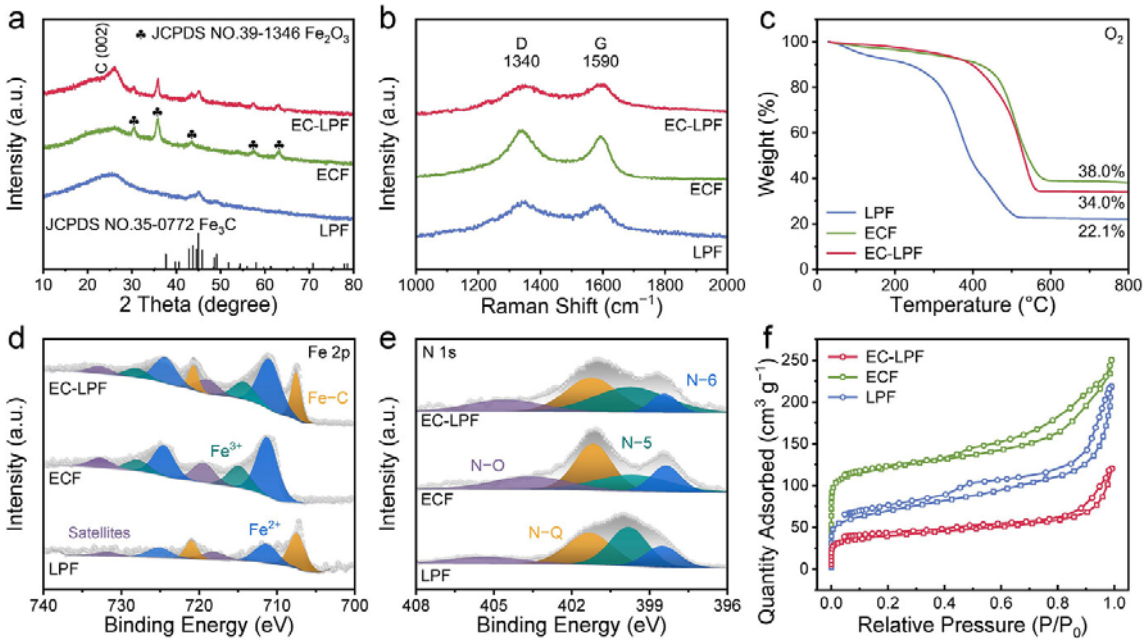

Figure 2. a) XRD patterns, b) Raman spectra, c) TG curves, high-resolution XPS spectra of d) Fe 2p and e) N 1s, and f) nitrogen adsorption and desorption isotherms of EC-LPF, ECF, and LPF.

The lithium-ion storage performance and lithiophilicity of self-supporting electrodes are characterized using a dual electrode configuration in conjunction with lithium foil. These cells are initially cycled within a range of 0−3 V, and the typical charge−discharge curve of the initial battery cycle is shown in **Figure** 3a. The electrode containing the electrochemically active Fe_2O_3 substrate achieves a substantial reversible capacity, particularly EC-LPF, with a specific capacity of 897 mAh g^{-1}. Furthermore, the solid electrolyte interphase (SEI) is formed by a portion of the capacity. Post stabilization, EC-LPF, ECF, and LPF exhibit specific capacities of 695, 757, and 337 mAh g^{-1} (Figure S6, Supporting Information), respectively, with a Coulombic efficiency of up to 99%. The corresponding redox peak around 1 V, observable through the dQ/dV curves in Figure 3b, can be ascribed to the contribution of Fe_2O_3 in storing lithium ions. Upon lithium intercalation, Fe_2O_3 successfully transformed into Fe (Figure 3c), as reported in the literature.[23] Notably, due to exposure to air, Li_2O has converted into LiOH. Additionally, the high-resolution TEM image (Figure 3d) further reveals the retention of Fe_3C grains amidst numerous graphitized carbon layers. The presence of cubic Fe $(Im\bar{3}m)$ is corroborated by the orientation along the $[1\bar{1}0]$ zone axis, as confirmed by FFT analysis.

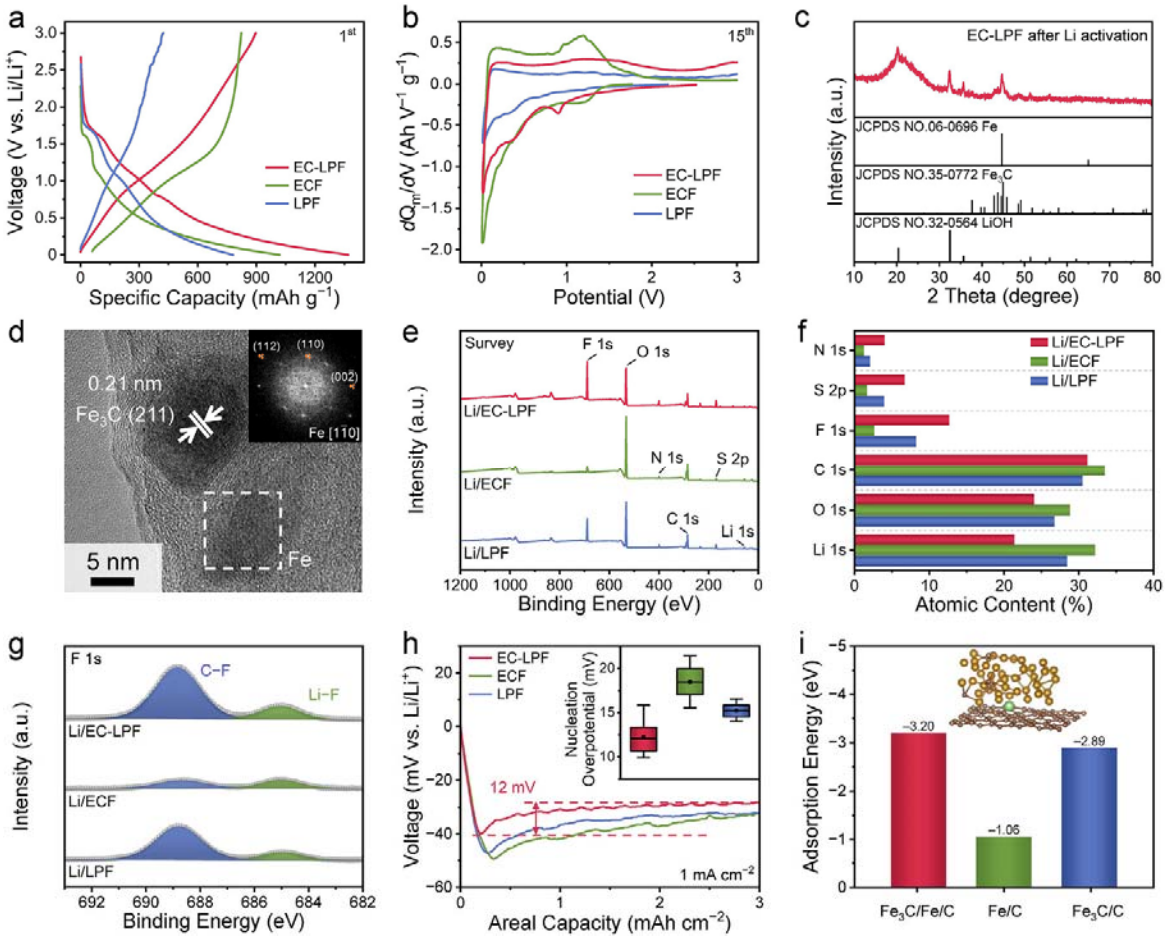

Figure 3. a) Charge–discharge curve of the first activation of the self-supporting electrode. b) The dQ/dV curve of the self-supporting electrode after 15 cycles. c) XRD pattern and d) TEM image of EC-LPF in lithium intercalated state after Li activation, inset: corresponding FFT pattern of highlighted squared region. e) Typical XPS survey spectra, f) atomic chemical composition obtained from XPS, and g) high-resolution XPS spectra of F 1s for self-supporting electrodes after lithium activation. h) Deposition curves of Li on self-supporting electrodes, inset: statistical nucleation overpotential diagram. i) The adsorption energy of Li on interface sites of composites.

Subsequently, the surface chemical structure and morphology of the electrode post-lithiation were examined. XPS analysis reveals an enrichment of inorganic components within SEI derived from EC-LPF. The survey spectrum depicted in Figure 3e indicates that the SEI on the self-supporting electrode is composed of elements Li, C, N, O, F, and S, with atomic concentrations detailed in Figure 3f and Table S1 (Supporting Information). A significant presence of lithium is observed, originating not only from the SEI but also from metallic lithium, as illustrated in Figure S7a (Supporting Information). This metallic lithium fraction is non-detachable, leading to the formation of dead lithium. Specifically, the composition of lithium metal decreases in the order of Li/ECF, Li/LPF, and Li/EC-LPF. Additionally, the substantial presence of C and O elements points to an organic SEI composition consisting of $RCOO^-$ and R_2CO^-, as corroborated by high-resolution C 1s spectra (Figure S7b, Supporting Information).[24] Conversely, the abundance of F and S elements in Li/EC-LPF suggests the existence of more robust inorganic SEI components.[25] A thorough analysis of the F 1s spectrum in Figure 3g shows peaks at 685.0 and 688.8 eV, which can be classified as Li–F and C–F, respectively.[26] Clearly, Li/EC-LPF and Li/LPF have higher SEI components containing

F compared to Li/ECF. The higher LiF content in Li/EC-LPF (1.8 at%) and Li/LPF (1.05 at%) compared to Li/ECF (0.92 at%), may be attributed to the catalytic effect of the electrode.[27] This helps to achieve a compact and stable SEI structure, thereby optimizing the lithium metal deposition/stripping process.[28] SEM observations of the SEI morphology on self-supporting electrodes reveal that EC-LPF possesses a uniformly thick SEI film (Figure S8, Supporting Information). In contrast, LPF and ECF display irregular microscopic protrusions on their surfaces, with a notable increase in fiber diameter, nearly doubling in size compared to the original fiber structure. These observations suggest that ECF possesses inferior lithiophilicity, which leads to the formation of less robust SEI structures. In comparison, LPF exhibits a relatively higher degree of lithiophilicity. EC-LPF, however, demonstrates the most favorable lithiophilicity and a stable SEI structure. This characteristic is beneficial for establishing a uniform lithium-ion flux across the electrode, contributing to the creation of a reliable lithium metal anode. Moreover, even after multiple cycles of lithium deposition and stripping, the particles within the fibers remain well-preserved (Figure S9, Supporting Information). This preservation of particles is an indicator of the robustness of the electrode material and its potential for long-term stability and high performance in lithium metal batteries.

Furthermore, the typical lithium deposition voltage profiles of EC-LPF, ECF, and LPF electrodes are presented in Figure 3h at a current density of 1 mA cm^{-2}. EC-LPF shows a nucleation overpotential of 12 mV, significantly lower than that of ECF and LPF. Statistical analysis of nucleation overpotential in the illustration also demonstrates that EC-LPF is lower than ECF (17 mV) and LPF (15 mV). DFT calculations were performed using Fe_3C, Fe crystals, and a graphene sheet to construct models representing the microstructure between Fe_3C or lithiated Fe_2O_3 particles and carbon nanofiber (Figure S10, Supporting Information). Subsequently, lithium atoms were introduced into the interface sites between the iron-based crystals and graphene (Figure S11, Supporting Information), as adsorption at heterogeneous interfaces is more favorable than surface adsorption.[29] Figure 3i shows that the introduction of graphene greatly improves the material's adsorption energy for lithium at the heterostructure interface. Furthermore, the Fe_3C/Fe composite material achieves an optimal adsorption energy (−3.20 eV). The aforementioned results demonstrate that the heterogeneous structure combining Fe_3C and Fe_2O_3 further amplifies its lithiophilicity.

The morphological evolution of Li metal deposition/stripping by self-supporting electrodes was further investigated using SEM. With the lithium deposition amount controlled at 2.5 mAh cm^{-2} and a current density is 0.5 mA cm^{-2}, the voltage curve is shown in Figure S12a (Supporting Information). Electrodes at the initial stage of lithium deposition (Stage I), the end stage of lithium deposition (Stage II), and the stage post-lithium stripping (Stage III) were selected for characterization (Figure S12b–d, Supporting Information). During Stage I, EC-LPF fibers appear smooth and hazy, indicating a uniform SEI layer. In contrast, ECF fiber membranes exhibit a few black blocks on the surface, attributable to a high nucleation barrier leading to the concentrated precipitation of metallic lithium. During Stage II, these black blocks expand and thicken, forming island-shaped metallic lithium. LPF also shows similar island-like metallic lithium in Stage II, but EC-LPF significantly mitigates this issue. At Stage III, these metallic lithium ions are almost entirely stripped, reverting to their original morphology prior to deposition (Figure S13, Supporting Information). Post-stripping, a small amount of metallic lithium remains in LPF fibers. The thickness of island metallic lithium on the ECF surface has decreased, but a considerable amount of dendritic lithium remains within the fibers, unstripped. This is consistent with the aforementioned XPS results post-activation. The large pores of electrospun fiber membranes enhance electrolyte penetration, and the presence of iron oxide improves the wettability of iron carbide (Figure S14, Supporting Information), thereby

reducing concentration polarization and the deposition of lithium metal on the electrode surface.

The electrochemical endurance and reversibility of the self-supporting electrodes as LMAs were initially assessed using a symmetrical battery setup. The Li/EC-LPF, Li/ECF, and Li/LPF electrodes, were pre-plated with 3 mAh cm^{-2} lithium on EC-LPF, ECF, and LPF at a current density of 1 mA cm^{-2}, respectively. **Figure** 4a illustrates the voltage hysteresis associated with the plating and stripping of metallic Li in the symmetric cell, conducted at a current of 1 mA cm^{-2} for a capacity of 1 mAh cm^{-2}. The Li/EC-LPF symmetric battery demonstrates the lowest overpotential and superior cycling stability, enduring for up to 960 h. The minimum overpotential recorded for the Li/EC-LPF was 12 mV, outperforming the Li/ECF at 15 mV and the Li/LPF at 21 mV. After 950 h, an increase in voltage polarization for the Li/EC-LPF symmetric batteries was observed, likely due to the qualitative changes from the continuous depletion of active lithium and the accumulation of dead lithium, a phenomenon that intensifies over extended cycling periods. This increase in polarization, however, confirms the absence of false positives in long-term performance indicators that might be caused by battery hard short circuits, as validated by the post-cycling Electrochemical Impedance Spectroscopy (EIS) (Figure S15a, Supporting Information).[30] In succession, the Li/ECF and Li/LPF symmetric batteries show escalating voltage hysteresis throughout cycling, culminating in failure after 320 and 640 h, respectively. Under identical current density and capacity conditions, the Li||EC-LPF half-cell demonstrates the highest CE of over 97% across 200 cycles at a 100% depth of discharge (Figure 4b). In contrast, the Li||ECF and Li||LPF half-cells exhibit shorter cycle lifetimes of 80 and 100 cycles, respectively, with an average CE of ≈96%. Even when subjected to a current density of up to 3 mA cm^{-2}, the voltage hysteresis of the Li/EC-LPF symmetric cells remains stable for 400 h (Figure 4c), a performance significantly superior to that of the Li/LPF (150 h) and Li/ECF (100 h). The magnified voltage curve and EIS (Figure S15b, Supporting Information) confirm low electrochemical polarization (24 mV) and stable cycling. These results underscore the EC-LPF host's ability to significantly bolster the reversibility of Li metal deposition and stripping. This enhancement is particularly advantageous, demonstrating its lithiophilic superiority, when compared to other lithium metal anode reports from the past 4 years (Figure 4d; Table S2, Supporting Information).

The high current performance of symmetric batteries was further evaluated through rate testing at a capacity of 1 mAh cm^{-2} (Figure 4e). Specifically, the Li/EC-LPF symmetric battery displays stable voltage polarization of 12, 25, 33, 38, and 41 mV at 1, 2, 3, 5, and 10 mA cm^{-2}, respectively. Conversely, as the rate increases, the polarization of the Li/LPF and Li/ECF symmetric batteries escalated due to their higher lithium diffusion barrier. The reaction kinetics at the electrode interface of the lithiophilic host were further investigated using Tafel curves.[31] The exchange current density (j_0) for the Li/EC-LPF symmetric batteries is 4.98 mA cm^{-2}, as shown in Figure 4f and Figure S16 (Supporting Information), surpassing that of the Li/LPF (3.86 mA cm^{-2}) and Li/ECF (2.59 mA cm^{-2}). This finding indicates a marked improvement in charge transfer capability at the electrode/electrolyte interface within the Li/EC-LPF symmetric batteries, a result of low electrochemical impedance and high-quality SEI. Collectively, these results highlight that the Fe_3C/Fe_2O_3 heterostructure host significantly ameliorates the Li deposition/stripping overpotential and enhances stability in symmetric batteries.

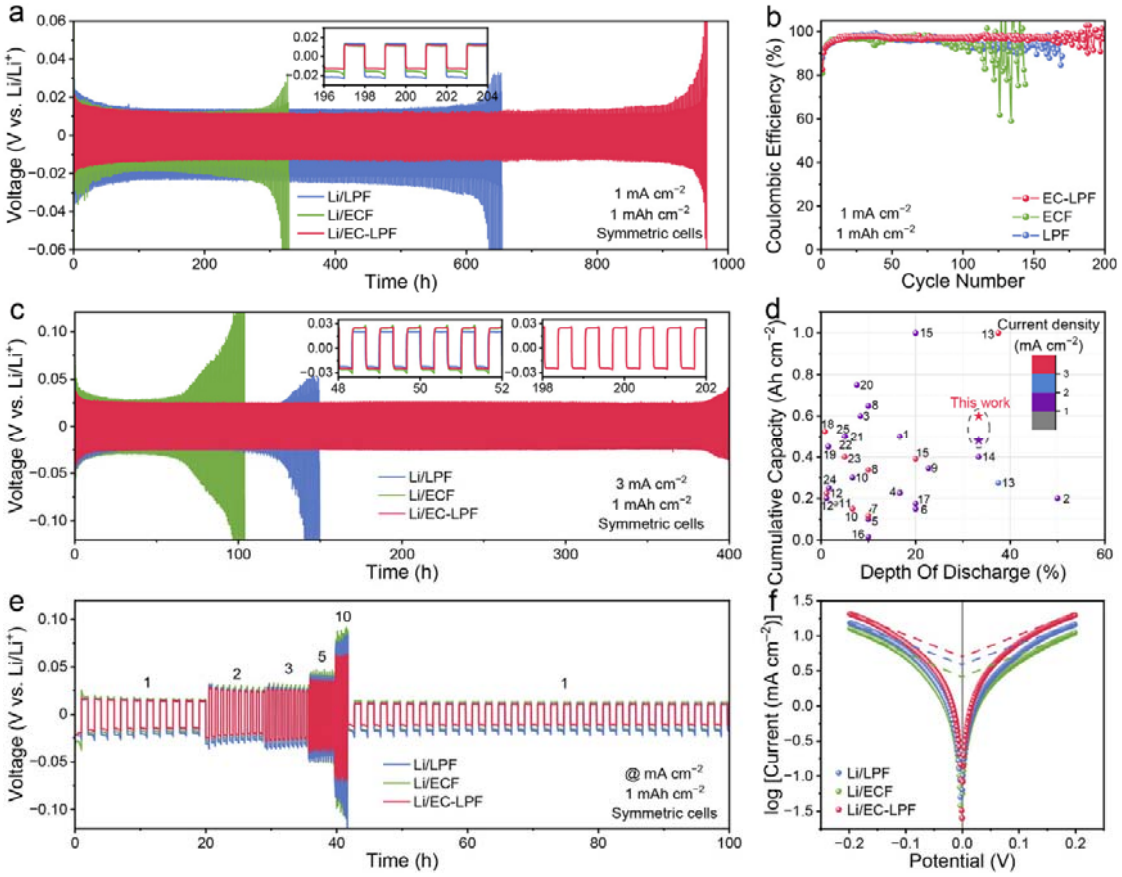

Figure 4. a) Voltage hysteresis of metallic Li plating/stripping in the symmetric cells of fibers symmetric cell at 1 mA cm^{-2} for 1 mAh cm^{-2}. b) Coulombic efficiency of Li||CNF half cells at 1 mA cm^{-2} with the deposition capacity of 1 mAh cm^{-2}. c) Voltage hysteresis of metallic Li plating/stripping in the symmetric cells of fibers symmetric cell at a current of 3 mA cm^{-2} for 1 mAh cm^{-2}. d) Comparison diagram of electrochemical performance of symmetric lithium metal batteries. e) Rate performance at various current densities. f) The Tafel plots in symmetric cells with a scan rate of 1.0 mV s^{-1}.

To extend the investigation of the unique attributes of EC-LPF heterogeneous material in lithium metal batteries, its performance in a full cell configuration was assessed by integrating it with commercial $LiFePO_4$ cathodes. Due to its flat and stable charge and discharge plateau, $LiFePO_4$ serves as an ideal candidate for evaluating voltage hysteresis induced by the anode. The positive electrode was designed with a capacity of 1 mAh cm^{-2}, and the N/P ratio was maintained at 2. To mitigate the potential risk of decomposition of ether-based electrolytes under high voltage, a voltage range of 2–3.7 V has been adopted.[32] As illustrated in **Figure** 5a, the $LiFePO_4$||Li/EC-LPF configuration shows the highest initial discharge capacity (139 mAh g^{-1}), retaining 66% after 500 cycles at a rate of 1C (1C = 170 mA g^{-1}), with a CE of 99.9%. In contrast, the $LiFePO_4$||Li/LPF and $LiFePO_4$||Li/ECF exhibit notable performance degradation at the 200 and 160 cycles, respectively. This decline is attributed to the accumulation of dead lithium on the anode surface, resulting in sudden drop in full battery performance (Figure S17, Supporting Information). The superior low polarization of the EC-LPF is further evident upon comparing the capacity–voltage curves (Figure S18, Supporting Information). The $LiFePO_4$||Li/EC-LPF battery demonstrates significantly lower voltage hysteresis of 98 mV during charge and discharge, outperforming the $LiFePO_4$||Li/LPF (123 mV) and $LiFePO_4$||Li/ECF (157 mV). This advantage is linked to the adept lithium plating/stripping ability and elevated lithium-ion diffusion rate of EC-LPF. An intriguing

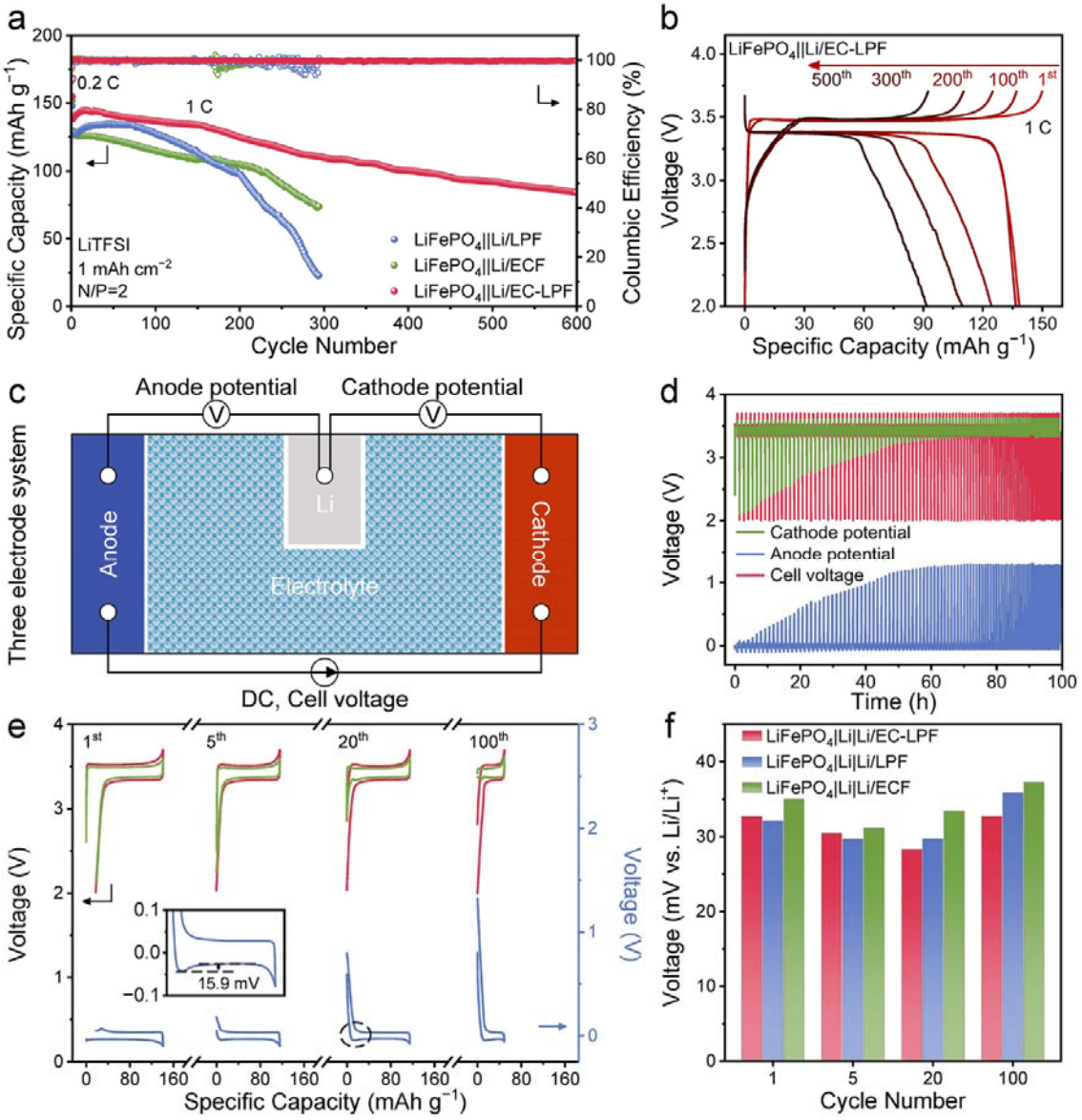

Figure 5. a) Long-term cycling of $LiFePO_4$ full batteries with different anodes at 1C, and b) corresponding voltage profiles. c) Schematic diagram of the testing principle for a three electrode system. d) The voltage distribution curve of $LiFePO_4$|Li|Li/EC-LPF full cell and e) the potential distribution of each electrode in a three electrode system, with enlarged curves for specific cycles. f) The potential of lithium metal anode in a three electrode system for 1, 5, 20, and 100 cycles.

observation is that in the subsequent cycle of $LiFePO_4$||Li/ECF, a minor bulge emerges ahead of the charging platform (Figure S19, Supporting Information), indicative of the depletion of metal lithium in the anode. Then, lithium ions from the cathode re-deposit on the anode during charging. The poor lithiophilicity of the ECF leads to continuous accumulation of dead lithium, accelerating the full cell performance decline. Conversely, the $LiFePO_4$||Li/LPF batteries have no significant bulges except for capacity decay. In addition, as the cycle progresses (Figure 5b), the charge and discharge curves of the $LiFePO_4$||Li/EC-LPF and $LiFePO_4$||Li/ECF undergo deformation. This can be ascribed to the gradual consumption of metallic lithium, with the lithium-ion capacity pre-stored in Fe_2O_3 being progressively replenished into the cycle. The $LiFePO_4$||EC-LPF full battery also demonstrates the best cycling stability at an N/P ratio of 0,

retaining 87% of its initial capacity after 100 cycles at 1C (Figure S20, Supporting Information).

This perspective is further corroborated through three-electrode testing, which is advantageous because it can separate the voltage changes of the positive and negative electrodes, offering a clearer analysis of the electrode failure mechanisms (Figure 5c). A button-type three-electrode battery was assembled using homemade lithium reference electrodes, with the structure and positioning of the lithium reference electrode detailed in Figure S21 (Supporting Information). The voltage distribution curve of the $LiFePO_4$|Li|Li/EC-LPF three-electrode cell is depicted in Figure 5d. It is observed that while the electrode potentials of the cathode and anode display a decreasing and increasing trend, respectively, the cell voltage remains stable. Initially, the cathode exhibits a characteristic $LiFePO_4$ charging/discharging platform, and the anode shows a voltage profile akin to that of a symmetrical battery (Figure 5e). After 20 cycles, a notable increase in anode potential is detected, and the cathode potential deviates from its initial state, indicating complete stripping of anode metal lithium. Following that, metallic lithium re-deposits at the anode, with a nucleation overpotential of 15.9 mV, outperforming comparative sample (Figure S22, Supporting Information). During discharge, when the lithium metal capacity of the anode is insufficient to maintain a complete cycle of the cathode, the lithium-ion capacity within the system is released to allow continued lithium intercalation into the cathode until the discharge cutoff voltage is reached. Consequently, lithium ions pre-stored in Fe_2O_3 become active, corresponding to a capacity above 0.1 V. Voltage fluctuations below 0.5 V in the Li/LPF and disappear in subsequent cycles (Figure S23, Supporting Information), potentially due to unexpected side reactions.[33] As Fe_2O_3 releases more capacity, the voltage curve of the full battery begins to show a gradual trend deviation from the original sharp rise/drop. Compared to Li/EC-LPF, Li/ECF displays earlier lithium metal depletion due to inferior lithiophilicity. Li/LPF does not deliver the same voltage changes but suffers from rapid capacity decay. By 100 cycles, incomplete charging of the positive electrode is observed, indicating that failure is primarily due to lithium loss in the anode. This gradual change provides a buffer for the detection of open-circuit voltage and facilitates the calibration of the battery's state of charge.[34] Similar phenomena are also observed in carbonate based electrolytes (Figure S24, Supporting Information) and NCM full cells (Figure S25, Supporting Information). Moreover, the three-electrode configuration facilitates a more direct assessment of the negative electrode potential, revealing the actual contribution of overpotential from the lithium metal anode during cycling. Electrodes containing the Fe_3C substrate, such as Li/EC-LPF, demonstrate superior performance in the cycling process of the metallic lithium anode (Figure 5f), with an overpotential of 28 mV, better than Li/LPF (30 mV) and Li/ECF (33 mV). The EC-LPF host, with its lowest overpotential and pre-stored lithium-ion capacity, significantly extends the full battery cycle life.

The dynamic mechanism of the EC-LPF heterogeneous host in the full battery was then investigated. In the C-rate test, the $LiFePO_4$||Li/EC-LPF battery delivers high specific capacities of 156, 155, 150, 140, and 123 mAh g^{-1} at 0.2, 0.3, 0.5, 1, and 2C (**Figure** 6a), respectively. The $LiFePO_4$||Li/LPF also achieves commendable C-rate performance. As anticipated, the $LiFePO_4$||Li/ECF does not perform as well as batteries containing Fe_3C lithiophilic substances across all current densities, with significant capacity decay at 2C. This may be attributed to the overpotential of lithium deposition on the anode side, leading to electrochemical polarization that impedes the diffusion of lithium ions in the material, exacerbating concentration polarization, and resulting in limited capacity release. Cyclic voltammetry (CV) curves of the full batteries at various scanning rates are presented in Figure 6b, displaying the typical redox peaks of $LiFePO_4$ that tend to polarize with increasing

scanning rate. Moreover, compared with $LiFePO_4$||Li/LPF and $LiFePO_4$||Li/ECF (Figure S26, Supporting Information), the $LiFePO_4$||Li/EC-LPF full cell shows more intense redox peak, suggesting a higher reversible capacity. The charge−discharge voltage hysteresis can be quantified by calibrating the peak positions of each scanning rate in the CV, as depicted in Figure 6c.[35] The voltage hysteresis of the $LiFePO_4$||Li/EC-LPF consistently remains the lowest, for instance, it is only 319 and 690 mV at 0.2 and 2.0 mV s^{-1}, respectively, followed by the $LiFePO_4$||Li/LPF (329 and 736 mV) and $LiFePO_4$||Li/ECF (385 and 864 mV). Furthermore, the power-law relationship between current response (i) and scanning rate (v),[36] was used to quantify their interdependence. Although $LiFePO_4$ operates on a traditional intercalation redox mechanism controlled by semi-infinite diffusion, the battery exhibits varying proportions of Faradaic reactions under anodic influence (Figure S27, Supporting Information). The full cell charge storage mechanism is predominantly dominated by semi-infinite diffusion, nevertheless the $LiFePO_4$||Li/EC-LPF demonstrates greater advantages in Faradaic storage. The promising kinetic mechanism of the $LiFePO_4$||Li/EC-LPF can be ascribed to the lower lithium nucleation overpotential at the anode and the accelerated deposition/stripping rate of metallic lithium on the anode side.

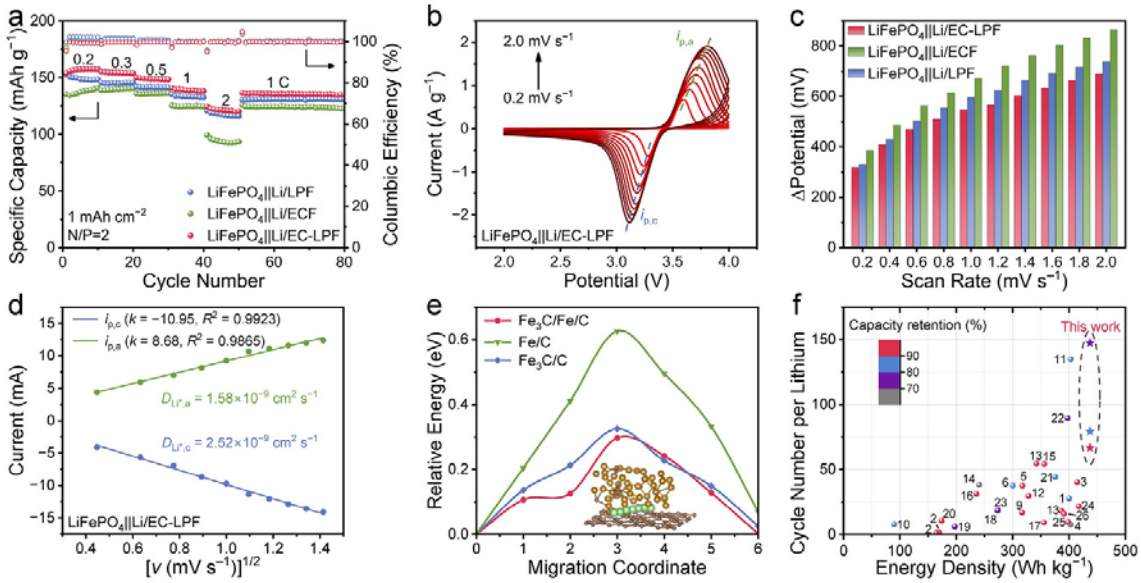

Figure 6. a) Rate performance. b) Typical CV curves of $LiFePO_4$||Li/EC-LPF under different scan rates of 0.2, 0.4, 0.6, 0.8, and 1.0 mV s^{-1}, and c) the corresponding linear fits of the peak currents. d) The voltage hysteresis diagrams from CV. e) The migration barrier of Li ion in the structure of EC-LPF, ECF, and LPF. f) Comparison diagram of electrochemical performance of $LiFePO_4$||Li full batteries.

The apparent lithium-ion diffusion coefficient (D_{Li^+}) was evaluated to characterize the diffusion kinetics of Li^+ in the full cell. A linear curve obtained by linearly fitting the peak current of CV confirms the enhanced lithium diffusion characteristics at the anode in the $LiFePO_4$||Li/EC-LPF (Figure 6d; Figure S28, Supporting Information). The galvanostatic intermittent titration technique (GITT) technique also supports these results (Figure S29, Supporting Information).[37] Specifically, the average D_{Li^+} of the $LiFePO_4$||Li/EC-LPF during discharge is 4.02×10^{-12} cm^2 s^{-1}, significantly improved compared to the $LiFePO_4$||Li/ECF (3.28×10^{-12} cm^2 s^{-1}). EIS also indicates that the $LiFePO_4$||Li/EC-LPF full cell has the lowest SEI resistance (R_{SEI}) and charge transfer resistance (R_{ct}) (Figure S30 and Table S3, Supporting Information). The inferior SEI of Li/ECF anode leads to additional polarization, resulting in a less favorable apparent diffusion coefficient. Moreover, as the current gradually increases, the

relatively poor lithium diffusion rate of the Li/ECF anode becomes the rate determining step, causing polarization and a decline in full battery performance at high current densities. The migration barrier of lithium ions was calculated using the optimal structure, and the corresponding relative energy distribution along the diffusion path is shown in Figure S31 (Supporting Information). The diffusion energy barrier for lithium crossing the Fe_3C/Fe heterostructure interface is the lowest (0.29 eV), indicating rapid diffusion characteristics (Figure 6e). Compared to lithium metal full batteries reported over the past 4 years, the $LiFePO_4$||Li/EC-LPF full batteries maintain significant advantages when considering energy density, cycle stability, and lithium utilization rate comprehensively (Figure 6f; Table S4, Supporting Information). Thanks to the superior lithium storage performance and adaptability to a lower N/P ratio of EC-LPF, considering the cathode material and lithium content, an energy density of up to 438 Wh kg^{-1} can be achieved. As a practical demonstration, $LiFePO_4$||Li/EC-LPF pouch cells were assembled and successfully powered an electronic badge (Figure S32, Supporting Information). These results confirm that Fe_3C/Fe_2O_3 heterostructure hosts with lithiophilic and electrochemical-activity can effectively regulate uniform lithium plating/stripping and improve the stability of lithium metal batteries.

3 Conclusion

In summary, the conversion–lithiophilicity strategy presented in this work has proven to be effective in enhancing lithium metal batteries performance. The integration of lithiophilic Fe_3C particles, achieved through electrospinning, resulted in low nucleation overpotential (12 mV) and uniform lithium deposition devoid of dendrite formation. The electrochemically active Fe_2O_3 component provided a reserve capacity, mitigating dead lithium expansion and extend battery lifespan. A comprehensive study on Li storage characteristics, nucleation mechanisms, and DFT calculations confirmed the benefits of the heterogeneous host. The $LiFePO_4$||Li/EC-LPF full cell demonstrated impressive performance, with rapid kinetics (124 mAh g^{-1} at 2C) and an unmatched cycle life exceeding 300 cycles at 1C, corresponding to an energy density of 438 Wh kg^{-1} (calculated based on the cathode material and lithium content). In theory, any material based on conversion reactions can achieve this effect. However, due to their unique potentials and other characteristics, different conversion materials will exhibit slight variations. Further exploration and experimentation are required to tailor them to specific systems. This innovative strategy is highly promising for the future advancement of high-performance lithium metal batteries.

Acknowledgements

This work was supported by the National Natural Science Foundation of China (22075141, 22101132, 22279016, 52131306, 92472117, and 52371226), the Scientific and Technological Innovation Special Fund for Carbon Peak and Carbon Neutrality of Jiangsu Province (BK20220039), and Jiangsu Provincial Founds for Natural Science Foundation (BK20170793, BK20180015 and BK20210311). The authors acknowledged the Center for Microscopy and Analysis at Nanjing University of Aeronautics and Astronautics.

Conflict of Interest

The authors declare no conflict of interest.

Data Availability Statement

The data that support the findings of this study are available from the corresponding author upon reasonable request.

References

1 a) F. Duffner, N. Kronemeyer, J. Tübke, J. Leker, M. Winter, R. Schmuch, *Nat. Energy* 2021, 6, 123;

b) X. Lian, N. Xu, Y. Ma, F. Hu, H. Wei, H. Y. Chen, Y. Wu, L. Li, D. Li, S. Peng, *Chem. Eng. J.* 2021, 421, 127755;

c) J. Ling, R. Kunwar, L. Li, S. Peng, I. I. Misnon, M. H. Ab Rahim, C.-C. Yang, R. Jose, *eSciece* 2022, 2, 347;

d) X.-T. Li, J. Chou, Y.-H. Zhu, W.-P. Wang, S. Xin, Y.-G. Guo, *eScience* 2023, 3, 100121.

2 a) C. Jin, T. Liu, O. Sheng, M. Li, T. Liu, Y. Yuan, J. Nai, Z. Ju, W. Zhang, Y. Liu, Y. Wang, Z. Lin, J. Lu, X. Tao, *Nat. Energy* 2021, 6, 378;

b) C. Wang, C. Yang, Y. Du, Z. Guo, H. Ye, *Adv. Funct. Mater.* 2023, 33, 2303427;

c) Z. Huang, X. Zheng, H. Liu, J. Huang, Y. Xu, X. Xu, Y. Dou, D. Yuan, Z. Li, S. X. Dou, H. K. Liu, S. Chou, C. Wu, *Adv. Funct. Mater.* 2024, 34, 2302062;

d) H. Zhang, R. Hu, S. Feng, Z. Lin, M. Zhu, *eScience* 2023, 3, 100080.

3 a) Z. Wang, Z. Du, Y. Liu, C. E. Knapp, Y. Dai, J. Li, W. Zhang, R. Chen, F. Guo, W. Zong, X. Gao, J. Zhu, C. Wei, G. He, *eScience* 2024, 4, 100189;

b) P. Albertus, S. Babinec, S. Litzelman, A. Newman, *Nat. Energy* 2018, 3, 16.

4 a) T. Krauskopf, F. H. Richter, W. G. Zeier, J. Janek, *Chem. Rev.* 2020, 120, 7745;

b) W. Cao, Q. Li, X. Yu, H. Li, *eScience* 2022, 2, 47;

c) H. Mao, W. Yu, Z. Cai, G. Liu, L. Liu, R. Wen, Y. Su, H. Kou, K. Xi, B. Li, H. Zhao, X. Da, H. Wu, W. Yan, S. Ding, *Angew. Chem., Int. Ed.* 2021, 60, 19306.

5 a) X. He, K. Zhang, Z. Zhu, Z. Tong, X. Liang, *Chem. Soc. Rev.* 2023, 53, 9;

b) A. Jia, J. Chao, C. Qin, X. Guo, G. Q. Yuan, J. Liu, H. Pang, *Chem. Eng. J.* 2024, 480, 148103.

6 N. Zhu, Y. Yang, Y. Li, Y. Bai, J. Rong, C. Wu, *Carbon Energy* 2024, 6, e423.

7 G. Yang, Z. Liu, S. Weng, Q. Zhang, X. Wang, Z. Wang, L. Gu, L. Chen, *Energy Storage Mater.* 2021, 36, 459.

8 a) J. Zhu, C. Yan, G. Li, H. Cheng, Y. Li, T. Liu, Q. Mao, H. Cho, Q. Gao, C. Gao, M. Jiang, X. Dong, X. Zhang, *Energy Storage Mater.* 2024, 65, 103111;

b) C. Li, M. Qiu, R. Li, X. Li, M. Wang, J. He, G. Lin, L. Xiao, Q. Qian, Q. Chen, J. Wu, X. Li, Y.-W. Mai, Y. Chen, *Adv. Fiber Mater.* 2022, 4, 43.

9 a) Y. S. Feng, Y.-N. Li, P. Wang, Z. P. Guo, F.-F. Cao, H. Ye, *Angew. Chem., Int. Ed.* 2023, 62, 202310132;

b) H. Kwon, H.-J. Choi, J.-k. Jang, J. Lee, J. Jung, W. Lee, Y. Roh, J. Baek, D. J. Shin, J.-H. Lee, N.-S. Choi, Y. S. Meng, H.-T. Kim, *Nat. Commun.* 2023, 14, 4047.

10 Y. Lu, L. Yu, X. W. Lou, *Chem* 2018, 4, 972.

11 J. Xu, X. Cai, S. Cai, Y. Shao, C. Hu, S. Lu, S. Ding, *Energy Environ. Mater.* 2023, 6, e12450.

12 P. Shi, L. P. Hou, C. B. Jin, Y. Xiao, Y. X. Yao, J. Xie, B. Q. Li, X. Q. Zhang, Q. Zhang, *J. Am. Chem. Soc.* 2022, 144, 212.

13 a) S. Qian, H. Chen, M. Zheng, Y. Zhu, C. Xing, Y. Tian, P. Yang, Z. Wu, S. Zhang, *Energy Storage Mater.* 2023, 57, 229;

b) B. Acebedo, M. C. Morant-Miñana, E. Gonzalo, I. Ruiz de Larramendi, A. Villaverde, J. Rikarte, L. Fallarino, *Adv. Energy Mater.* 2023, 13, 2203744.

14 C. Tian, F. Lin, M. M. Doeff, *Acc. Chem. Res.* 2018, 51, 89.

15 a) P. Bhattacharya, M. Kota, D. H. Suh, K. C. Roh, H. S. Park, *Adv. Energy Mater.* 2017, 7, 1700331;

b) W. Zhang, Z. Xie, M. Zheng, H. Hu, Y. Xiao, Y. Liu, Y. Liang, *Energy Storage Mater.* 2020, 29, 300.

16 a) Y. Zhang, Q. Wan, N. Yang, *Small* 2019, 15, 1903780;

b) T. Ji, L. Chen, M. Schmitz, F. S. Bao, J. Zhu, *Green Chem.* 2015, 17, 2515.

17 a) S. Zhou, C. Fu, Z. Chang, Y. Zhang, D. Xu, Q. He, S. Chai, X. Meng, M. Feng, Y. Zhang, J. Lin, A. Pan, *Energy Storage Mater.* 2022, 47, 482;

b) B. Sun, Q. Zhang, W. Xu, R. Zhao, H. Zhu, W. Lv, X. Li, N. Yang, *Nano Energy* 2022, 94, 106937.

18 N. Kim, H. Cha, S. Chae, T. Lee, Y. Lee, Y. Kim, J. Sung, J. Cho, *Energy Environ. Sci.* 2023, 16, 2505.

19 Z. Du, W. Guan, C. He, Y. Liu, W. Ai, *Energy Storage Mater.* 2024, 65, 103191.

20 a) X. Cui, L. Gao, S. Lei, S. Liang, J. Zhang, C. D. Sewell, W. Xue, Q. Liu, Z. Lin, Y. Yang, *Adv. Funct. Mater.* 2021, 31, 2009197;

b) X. Li, J. Su, Z. Li, Z. Zhao, F. Zhang, L. Zhang, W. Ye, Q. Li, K. Wang, X. Wang, H. Li, H. Hu, S. Yan, G. X. Miao, Q. Li, *Sci. Bull.* 2022, 67, 1145.

21 a) X. Chen, X. R. Chen, T. Z. Hou, B. Q. Li, X. B. Cheng, R. Zhang, Q. Zhang, *Sci. Adv.* 2019, 5, eaau7728;

b) J. Lee, S. H. Choi, H. Qutaish, Y. Hyeon, S. A. Han, Y. U. Heo, D. Whang, J. W. Lee, J. Moon, M. S. Park, J. H. Kim, S. X. Dou, *Energy Storage Mater.* 2021, 37, 315.

22 J. Song, D. Yu, X. Wu, D. Xie, Y. Sun, P. Vishniakov, F. Hu, L. Li, C. Li, M. Y. Maximov, K. M. El-Khatib, S. Peng, *Chem. Eng. J.* 2022, 437, 135281.

23 a) Y. Yang, X. Fan, G. Casillas, Z. Peng, G. Ruan, G. Wang, M. J. Yacaman, J. M. Tour, *ACS Nano* 2014, 8, 3939;

b) M. Qin, Z. Zhang, Y. Zhao, L. Liu, B. Jia, K. Han, H. Wu, Y. Liu, L. Wang, X. Min, K. Xi, C. Y. Lao, W. Wang, X. Qu, R. V. Kumar, *Adv. Funct. Mater.* 2019, 29, 1902822;

c) B. Wang, J. S. Chen, H. B. Wu, Z. Wang, X. W. Lou, *J. Am. Chem. Soc.* 2011, 133, 17146.

24 a) J. Jiang, X. Hu, S. Lu, C. Shen, S. Huang, X. Liu, Y. Jiang, J. Zhang, B. Zhao, *Energy Storage Mater.* 2023, 54, 885;

b) X. Gao, Y. Sun, B. He, Y. Nuli, J. Wang, J. Yang, *ACS Energy Lett.* 2024, 9, 1141.

25 R. Lin, Y. He, C. Wang, P. Zou, E. Hu, X. Q. Yang, K. Xu, H. L. Xin, *Nat. Nanotechnol.* 2022, 17, 768.

26 X. Jian Hu, Y. Ping Zheng, Z. Wei Li, C. Xia, D. H. C. Chua, X. Hu, T. Liu, X. Bin Liu, Z. Ping Wu, B. Yu Xia, *Angew. Chem., Int. Ed.* 2024, 63, 202319600.

27 a) S. Tan, J.-M. Kim, A. Corrao, S. Ghose, H. Zhong, N. Rui, X. Wang, S. Senanayake, B. J. Polzin, P. Khalifah, J. Xiao, J. Liu, K. Xu, X.-Q. Yang, X. Cao, E. Hu, *Nat. Nanotechnol.* 2023, 18, 243;

b) X.-L. Zhang, L. Ma, Y.-P. Cai, J. Fransaer, Q. Zheng, *Matter* 2024, 7, 583.

28 a) C. Senthil, S. G. Kim, S. S. Kim, M. G. Hahm, H. Y. Jung, *Small* 2022, 18, 2200919;

b) X. Zhou, F. Liu, Y. Wang, Y. Yao, Y. Shao, X. Rui, F. Wu, Y. Yu, *Adv. Energy Mater.* 2022, 12, 2202323.

29 a) B. Yu, D. Chen, Z. Wang, F. Qi, X. Zhang, X. Wang, Y. Hu, B. Wang, W. Zhang, Y. Chen, J. He, W. He, *Chem. Eng. J.* 2020, 399, 125837;

b) A. Huang, Y. Wu, H. Huang, C. Li, Y. Sun, L. Li, S. Peng, *Adv. Funct. Mater.* 2023, 33, 2303111.

30 a) C. Wang, T. Deng, X. Fan, M. Zheng, R. Yu, Q. Lu, H. Duan, H. Huang, C. Wang, X. Sun, *Joule* 2022, 6, 1770;

b) D. Li, Y. Ouyang, Y. Xiao, Y. Xie, Q. Zeng, S. Yu, C. Zheng, Q. Zhang, S. Huang, *Adv. Funct. Mater.* 2024, 34, 2314296.

31 a) Z. Sun, Y. Wang, S. Shen, X. Li, X. Hu, M. Hu, Y. Su, S. Ding, C. Xiao, *Angew. Chem., Int. Ed.* 2023, 62, 202309622;

b) P. Liu, L. Miao, Z. Sun, X. Chen, Y. Si, Q. Wang, L. Jiao, *Angew. Chem., Int. Ed.* 2023, 62, 202312413.

32 a) J. G. Zhang, W. Xu, J. Xiao, X. Cao, J. Liu, *Chem. Rev.* 2020, 120, 13312;

b) L. Lin, H. Zheng, Q. Luo, J. Lin, L. Wang, Q. Xie, D.-L. Peng, J. Lu, *Adv. Funct. Mater.* 2024, 34, 2315201;

c) J. B. Goodenough, Y. Kim, *Chem. Mater.* 2010, 22, 587.

33 a) Z. Guo, Z. Xu, F. Xie, J. Jiang, K. Zheng, S. Alabidun, M. Crespo-Ribadeneyra, Y.-S. Hu, H. Au, M.-M. Titirici, *Adv. Mater.* 2023, 35, 2304091;

b) Y. Chen, B. Xi, M. Huang, L. Shi, S. Huang, N. Guo, D. Li, Z. Ju, S. Xiong, *Adv. Mater.* 2022, 34, 2108621.

34 a) M. R. Ramezani-al, M. Moodi, *J. Energy Storage* 2023, 67, 107605;

b) L. Ju, P. Long, G. Geng, Q. Jiang, *J. Energy Storage* 2024, 79, 110224.

35 J. He, Y. Tang, G. Liu, H. Li, M. Ye, Y. Zhang, Q. Yang, X. Liu, C. Li, *Adv. Energy Mater.* 2022, 12, 2202661.

36 a) H. Xu, W. He, Z. Li, J. Chi, J. Jiang, K. Huang, S. Li, G. Sun, H. Dou, X. Zhang, *Adv. Funct. Mater.* 2022, 32, 2111131;

b) Q. Zheng, S. Zhou, S. Tang, H. Zeng, Y. Tang, Z. Li, S. Liu, L. Xiao, L. Huang, Y. Qiao, S. G. Sun, H. G. Liao, *Angew. Chem., Int. Ed.* 2023, 62, 202303343.

37 J. Shi, P. Li, K. Han, D. Sun, W. Zhao, Z. Liu, G. Liang, K. Davey, Z. Guo, X. Qu, *Energy Storage Mater.* 2022, 51, 306.